In Situ Generation of Pd/PdO Nanoparticle Methane Combustion Catalyst: Correlation of Particle Surface Chemistry with Ignition

B. Van Devener,[†] S. L. Anderson,*,[†] T. Shimizu,[‡] H. Wang,[‡] J. Nabity,[§] J. Engel,[§] J. Yu,[§] D. Wickham,[||] and S. Williams[⊥]

Department of Chemistry, University of Utah, Salt Lake City, Utah 84112, Department of Aerospace and Mechanical Engineering, University of Southern California, Los Angeles, California 90089, TDA Research, Inc., 12345 W. 52nd Avenue, Wheat Ridge, Colorado 80033, Reaction Systems, LLC, 19039 E. Plaza Drive, 290, Parker, Colorado 80138, and Air Force Research Laboratory, Mail Stop PRAS, 1950 Fifth Street, WPAFB, Ohio 45433

Received: May 8, 2009; Revised Manuscript Received: October 6, 2009

Decomposition of a fuel-soluble precursor was used for in situ generation of Pd/PdO nanoparticles, which then catalyzed ignition of the methane/O_2/N_2 flow. To help understand the relationship between particle properties and activity, the composition, structure, and surface chemical state of the particles were determined by a combination of high-resolution transmission electron microscopy (HRTEM), electron diffraction, scanning transmission electron microscopy/energy dispersive X-ray spectroscopy (STEM/EDX), and X-ray photoelectron spectroscopy (XPS). The particles, collected under methane-free conditions, were found to be primarily crystalline, metallic Pd, with TEM results showing a narrow size distribution around 8 nm and scanning mobility particle sizing measurements (SMPS) indicating a median particle size of ~10 nm. The ignition temperature was lowered ~150 K by the catalyst, and we present evidence that ignition is correlated with formation of a subnanometer oxidized Pd surface layer.

I. Introduction

Supported palladium has frequently been used as a catalyst for methane combustion, with the metal typically supported in fixed-bed reactors. The extensive work on the kinetics of Pd oxidation and its relation to the catalytic activity has been reviewed.[1] More recently, Pd-based catalysts have been proposed to improve performance of propulsion platforms. Catalysts are needed both to enhance and control endothermic reactions in the fuel system for thermal management[2] and to enhance ignition and combustion rates. For combustion applications, the typical fixed-bed catalytic reactor approach is not possible because of the high flow velocities required. One proposed solution is to use fuel-soluble catalysts or catalyst precursors and inject them into the combustor with the fuel, generating a highly dispersed, unsupported catalyst in situ. Cryogenic methane has been proposed as a viable fuel because of its high density and specific energy content in comparison to hydrogen and jet fuels and low tendency toward coke formation.[3]

Nabity, Wickham, and co-workers reported several studies[4,5] in which fuel-soluble nanoparticles and organometallic compounds containing Pd were injected into a flow tube reactor as an aerosol, resulting in large decreases in ignition temperature for both methane and long-chain hydrocarbon combustion. Motivated by these results, Shimizu et al.[6] recently reported a flow tube reactor study of methane ignition, with and without injection of aerosols containing a Pd organometallic precursor compound. Reductions in ignition temperature of ~150 K were observed, and nanoparticles were observed in the exhaust and characterized by a combination of scanning mobility particle sizing (SMPS) and low-resolution transmission electron microscopy. Curiously, there appeared to be no significant differences in particle size or structure for particles formed at temperatures above and below the ignition temperature, and it was, therefore, unclear how the particles and their properties might relate to ignition.

Here we present detailed characterization of particles collected in those experiments, focusing on similarities and differences in the particle properties for reactor runs above and below the temperature where ignition was observed. The questions addressed are the nature of the Pd-containing species produced in the combustion environment, the nanoparticle formation mechanism, and the relation to the observed ignition behavior. One of the main questions is the oxidation state of the Pd, which has been shown to strongly affect activity for methane combustion.[1,7–12]

There have been a number of previous experiments using organometallic precursors in a combustion environment for nanoparticle synthesis. For example Nasibulin et al. have demonstrated nanoparticle synthesis using $Cu(acac)_2$ (copper(II) acetylacetonate) entrained in a N_2/O_2 flow and passed through a flow tube reactor, whereupon the organic ligands were burned off, leaving behind a vapor of Cu, which then condensed to form copper oxide nanoparticles.[13] Similarly, a number of different groups have used flame-based synthesis methods to prepare Pd-based combination catalysts,[14,15] as well as supported Pd catalysts.[16–22] Solution-based methods have frequently used Pd organometallics to prepare Pd-rich nanoparticles that were used in situ to catalyze organic reactions.[23–30]

Unsupported Pd particles have previously been shown to be effective combustion catalysts, in the gas phase, however, in those studies the particle generation and catalytic combustion

* To whom correspondence should be addressed. Phone: 801-585-7289. Fax: 801-581-8433. E-mail: anderson@chem.utah.edu.
[†] University of Utah.
[‡] University of Southern California.
[§] TDA Research, Inc.
[||] Reaction Systems, LLC.
[⊥] Air Force Research Laboratory.

10.1021/jp904317y CCC: $40.75 © 2009 American Chemical Society
Published on Web 11/09/2009

were done separately.[31–36] In the flow tube experiments of Shimizu et al.[6] the particles form as the fuel spray is pyrolyzed then catalyzes ignition in situ. The focus of this report is on the differences in properties for nanoparticles collected above and below the temperature where ignition was observed to try to understand the particle formation and catalyst activation processes.

II. Experimental Methods

The experimental details were described in detail by Shimizu et al.[6] Briefly, the reactor consists of a quartz tube (94 cm long, 1.7 cm i.d.) which passes through a tube furnace (Mellen SV12) with a test section length (L) of 76 cm. The reactor can reach temperatures of 1200 °C, which are monitored by K-type thermocouples mounted on the outside of the quartz tube. Temperatures measured in the gas flow under reacting conditions are typically ~100 °C lower than those for the reactor wall. Palladium was introduced as a toluene solution of palladium-2,2,6,6-tetramethyl-3,5-heptanedione ($Pd(THD)_2$), dispersed in N_2 as micrometer-size droplets by a cooled, concentric nozzle atomizer constructed of glass. After passing several impactors designed to remove large droplets, the droplet stream was mixed with a premixed N_2, O_2, and CH_4 flow (equivalence ratio = 0.4, O_2/N_2 = 0.84 mol) and entered the flow tube reactor. Evaporation and dissociation of the $Pd(THD)_2$ precursor (sublimation temperature ~150 °C at 0.01 Torr) follows as the gas heats, releasing Pd atoms or clusters, which grow into nanoparticles by the time the gas exits the reactor. For high enough temperatures, the nanoparticles catalyze methane ignition, and here we are interested in what properties of the nanoparticle correlate with ignition and what this may reveal about the mechanism.

Total reactor pressure was ~ 1 atm, and residence time at the temperatures of interest was ~1 s. Products exiting the reactor were diluted 8:1 in cold nitrogen gas in order to quench the reaction and minimize postreactor changes in the particles. The concentrations of the $Pd(THD)_2$ precursor in toluene were 12 000 ppm for all samples, and the catalyst loading in the gas flow was 1672 and 1687 $\mu g/g_{CH4}$ for the 500 and 700 °C reactor runs, respectively. The concentrations of CH_4 and CO_2 at the exit of the reactor were continuously monitored using an NDIR gas analyzer (California Analytical Instruments Model 200), which withdraws 2 L/min of the diluted exhaust gas. The size distributions of particles at the exit were measured using a scanning mobility particle sizer (TSI SMPS 3090). The residence time from the reactor exit to the SMPS inlet was 0.6 s. The particle size distribution was scanned over the range from 4.53 to 160 nm in diameter.

It is important to note that in experiments where ignition occurred, there was a large spike in gas temperature that would presumably cause substantial modification of the particle properties, in particular the particle surface chemistry of interest for ignition catalysis. To avoid this problem, in experiments where particles were collected for microscopy and surface anlaysis, the reactor flows contained only oxygen and nitrogen (without methane) but had total gas velocity (52.5 cm/s) and flow composition otherwise identical to the ignition experiments (mole fractions: 0.007 toluene, 0.420 O_2, and 0.573 N_2). Particles were collected for two different reactor temperatures, just below (500 °C) and above (700 °C) the temperature where ignition was observed when CH_4 was present.

In the original study, the measured average mobility diameters were in the ~25 nm range; however, comparison with TEM suggested the possibility that significant aggregation was occurring. For the present paper, the effects of aggregation were examined by modifying the reactor to allow more efficient dilution of the particle stream from the reactor prior to SMPS analysis. We used a venturi-like probe imbedded directly into the quartz flow tube, crossing the incoming reacting flow.

Particles were also collected on grids (Electron Microscopy Science HC200-CU) by exposing grids to the diluted exhaust flow, flowing parallel to the grid surface. The linear flow rate of the aerosol was 13 m/s over the grid. Under this condition, the flow is turbulent and the principal mechanism of particle collection is diffusion of the particles across the laminar boundary layer near the surface. As will be discussed below, diffusion-mediated collection biases against large particles, since the particle diffusivity is inversely proportional to the diameter squared.

High-resolution transmission electron microscopy (HRTEM) and selected area electron diffraction (SAED) was done using an FEI Technai F30 at 300 keV beam energy. Scanning transmission electron microscopy (STEM) analysis was performed on an FEI Technai F20 operated at 200 keV, with a high-angle annular dark field (HAADF) detector. The STEM was also used for energy dispersive X-ray (EDX) analysis of elemental compositions. Spectra were background-subtracted, integrated, and converted to elemental compositions using k-factors supplied by EDAX Inc. X-ray photoelectron spectra (XPS) were collected using the monochromatic Al Kα source (1486.7 eV) on a Kratos Axis Ultra DLD instrument.

Results and Discussion

There are several general points to be made before discussing the particle properties. As the N_2 flow in which the $Pd(THD)_2$/toluene aerosol is entrained mixes with the main $CH_4/O_2/N_2$ flow and enters the heated section of the reactor, the aerosol droplets are expected to evaporate rapidly (bp toluene = 111 °C, $T_{sublimation}$ $Pd(THD)_2 \approx 150$ °C), releasing the $Pd(THD)_2$ vapor into the flow. $Pd(THD)_2$ is a weakly bound coordination complex, expected to decompose at relatively low temperatures, releasing Pd atoms into the flow. As will be shown below, the Pd atoms nucleate to form nanoparticles, which catalyze ignition of the methane at 600 °C gas temperature (700 °C wall temperature).

One question is whether $Pd(THD)_2$ decomposition is fast enough at the temperatures of interest, so that nanoparticle growth is complete, or nearly so, before the exit of the flow tube. We note that the nanoparticle size distribution is, essentially, independent of reactor temperature from at least 500 to 800 °C. If the $Pd(THD)_2$ decomposition rate were a significant factor controlling nanoparticle nucleation and growth, we would expect the particle size distribution to change significantly over such a broad temperature range.

A. After Passage through the Reactor at 500 °C. The large-area TEM image in Figure 1 shows particles collected after passage through the flow reactor at 500 °C. Ignition of methane-containing flows was not observed at this temperature at any catalyst concentration examined. Even at low resolution, it can be seen that the larger particles are simply aggregates of smaller primary particles. Aggregates can form both in the gas phase prior to deposition and on the surface as particles are deposited. The spatial uniformity of particles collected over the area is indicative of particle deposition by a diffusion mechanism. The lower frame of Figure 1 shows the corresponding size distribution of the primary particles. For particles that appeared to be aggregates of smaller primary particles, the size distribution counts the sizes of the individual primary particles, rather than the aggregate size, within the resolution limit. Most

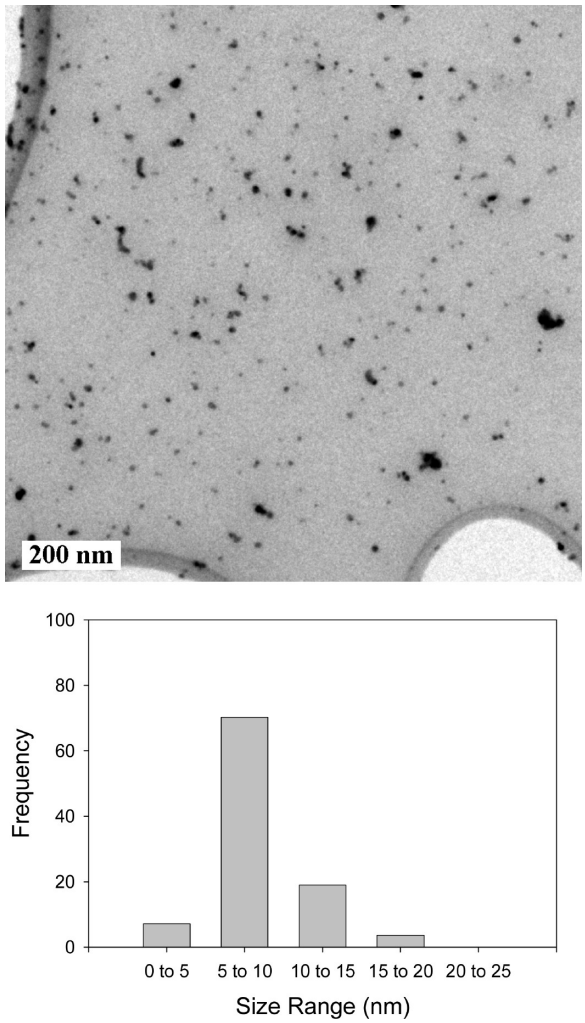

Figure 1. (Top) Low-magnification TEM image of $Pd(THD)_2$ catalyst after passage through reactor at 500 °C. (Bottom) Corresponding size distribution.

of the primary particles are between 5 and 10 nm in diameter with an average size of 8.3 nm. In the next section, we discuss evidence that most, or possibly all the aggregation takes place as the particles are deposited on the TEM grid.

The SAED pattern measured for this sample is shown in Figure 2. The brightest diffraction ring is closest to the center, typical of fcc materials.[37] Assigning the rings to particular lattice vectors must be done with caution because nanoscale particles can have significantly different lattice parameters than bulk material due to the large fraction of atoms at surfaces and grain boundaries. Fortunately, a study by Penner et al. on 5−10 nm Pd and PdO nanoparticles showed no significant changes in lattice parameters compared to the bulk materials.[38] Table 1 lists the lattice distances extracted from the SAED of the particles, together with reference values from the literature[38,39] for several materials of interest. The experimental values represent the average of several measurements, all which had a variance of less than 1%. Note the close match (<0.5% deviation) between most of the experimental distances and lattice parameters for Pd metal. The two short distances (1.120 and 0.893 Å) correspond to the very faint and diffuse outer rings, and we have not been able to assign them. Under the conditions of particle formation (500 °C, oxidizing conditions) formation of PdO is thermodynamically favorable;[40] thus, we looked carefully for evidence of PdO. The table also gives the PdO lattice

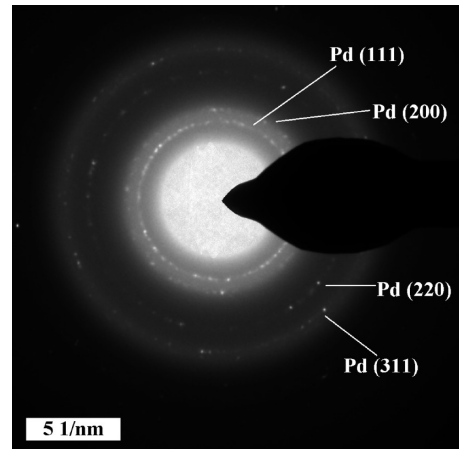

Figure 2. SAED pattern for $Pd(THD)_2$ catalyst after passage through reactor at 500 °C.

distances that best match the experimental distances, and it can be seen that overall pattern is much better matched by metallic Pd.

Typical high-resolution images, shown in Figure 3a and b, indicate a more complicated particle structure than that suggested by electron diffraction. Figure 3a shows a typical primary particle, roughly ∼10 nm in diameter with well developed lattice fringes. The 2.28 Å lattice spacing clearly corresponds to the spacing between Pd (111) planes (Table 1). This same spacing is seen in high-resolution images of most particles examined, confirming that the bulk of the particles is metallic Pd. The slight discrepancy in the distance measured from the images, relative to SAED, is simply measurement error. The spacing was measured by averaging the distances between successive peaks in the contrast profile taken along a line perpendicular to the fringes. Pixelation at the 800 k magnification used in the image results in some error in this measurement. Nevertheless, the discrepancy is small and the assignment is clear. A similar small discrepancy is seen when comparing other distances from the images with the SAED results.

Figure 3b shows an ∼50 nm particle with more complex structure. In addition to the two attached ∼10 nm particles, both indexed to Pd(111), the main body of the larger particle shows two different sets of fringes: one with *d*-spacings of 2.28 Å and another with *d*-spacings of 3.35 Å. 2.28 Å is just Pd(111) appearing again, but 3.35 Å is not a good fit to any Pd or PdO index. The most likely assignment is to either graphite or SiO_2 (see below), as indicated in Table 1. Moiré fringes are also apparent in the upper-right region of the main particle, indicating interference from two different sets of overlapping fringes. The obvious assignment would be to relate Moiré fringes to interference between the 2.28 and 3.35 Å spacings, however, observations made by Datye et al.[41] suggested that we should consider an alternative. They observed Moiré patterns resulting from interference between PdO(110) and Pd(200) planes in their study of Pd nanoparticles on alumina supports. Given that PdO is thermodynamically favored under conditions of this experiment,[42] such interferences might provide evidence that the particles are at least partly oxidized, despite lack of direct evidence in the SAED or HRTEM images. A general expression[37] for Moiré fringes caused by a combination of translational and rotational displacements of two overlapping lattices, was used to calculate the range of possible Moiré spacings that could result from Pd and PdO lattices:

TABLE 1: Comparison of SAED Results with Literature

exptl data and assignments			Pd[a]		PdO[a]		SiO_2[b]		graphite[b]	
d (Å) 500°	*d* (Å) 700°	lattice plane	*d* (Å)	lattice plane	*d* (Å)	lattice plane	*d* (Å)	lattice plane	*d* (Å)	lattice plane
2.234	2.245	Pd(111)	2.246	(111)	3.046	(100)	4.257	(010)	3.350	(002)
1.943	1.957	Pd(200)	1.945	(200)	2.667	(002)	3.342	(011)	1.675	(102)
1.369	1.370	Pd(220)	1.375	(220)	2.644	(101)	1.818	(112)	1.541	(103)
1.173	1.170	Pd(311)	1.173	(311)	2.153	(110)				
1.120	–	–			1.674	(112)				
0.893	–	–			1.536	(103)				
					1.522	(200)				
					1.335	(004)				
					1.332	(202)				

[a] Values of *d* and assignments for Pd and PdO taken from ref 11. [b] Values of *d* and assignments for SiO_2 and graphite from ref 12.

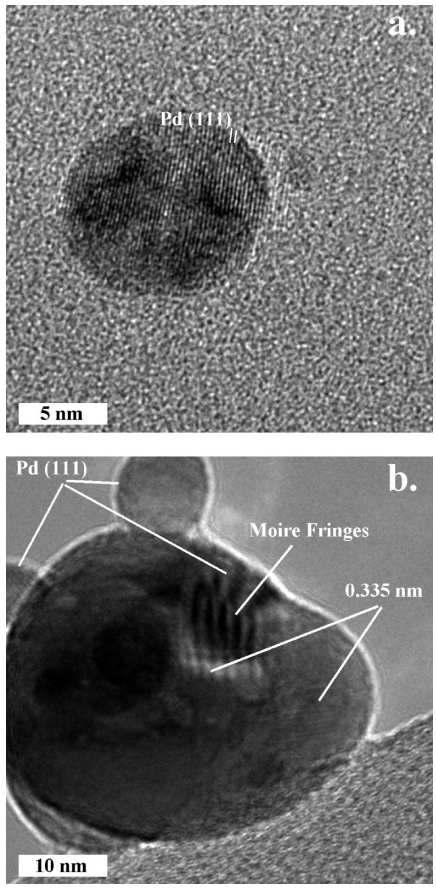

Figure 3. HRTEM images of $Pd(THD)_2$ catalyst after passage through reactor at 500 °C. (a) Small particle with Pd(111) lattice fringes; (b) group of particles with Moiré interference.

$$d_{gm} = \frac{d_1 d_2}{\sqrt{(d_1 - d_2)^2 + d_1 d_2 \beta^2}}$$

Here, d_{gm} is the spacing of the Moiré fringes, d_1 and d_2 are the spacing of the two interfering planes, and β is the angle between the planes. We examined all possible permutations of low index lattice planes from all species present or possibly present in the samples (Pd, PdO, graphite, SiO_2), and Table 2 summarizes only the best few fits to the observed spacing (16.51 Å). The best match (3% error) is an interference between Pd(200) with SiO_2(112). The best match for Pd/PdO is the Pd(200)/PdO(110) overlap identified by Datye et al.; however, the error is significantly worse (7.5%). We also used this approach to see how well we could fit the Moiré fringe spacing observed by Datye et al. (estimated by us from Figure 10 of the Datye paper[41]) to an interference between PdO(110) and Pd(200). As indicated in Table 2, the best fit differs from the estimated experimental spacing by ~13%.

TABLE 2: Moiré Fringe Measurements

this work d_{gm} measured 16.51		Datye et al.[a] d_{gm} measured 23.27
possible interfering planes	d_{gm} (Å) calcd	d_{gm} (Å) calcd
Pd(200)/SiO2	17.04	–
Pd(200)/PdO(110)	15.28	20.13
Pd(111)/Pd(101)	13.16	–
Pd(111)/PdO(200)	12.41	–

[a] Measured and calculated values are based on Figure 10 from ref 14.

SAED and HRTEM confirm the presence of metallic, crystalline Pd nanoparticles. STEM measurements using a HAADF detector coupled with small spot EDX were made to look for other constituents of the sample. Figure 4 shows three STEM images with corresponding atomic composition data for the indicated analysis areas summarized in Table 3. Image A shows a cluster of particles. With the HAADF detector, bright areas correspond to regions that are either thicker, or contain higher concentrations of high Z elements, or both. Note that there are three distinct brightness levels present in the image. There appears to be a very diffuse material that extends over much of the image, well outside the EDX analysis area indicated by the rectangular border. Inside the border, there is a collection of higher brightness areas, indicating an aggregate of particles. Note, however, that even within the grouping of particles, there are two distinct brightness levels. The highest contrast areas range from ~5 to ~20 nm in size, and these appear to be superimposed on larger 20 – 30 nm particles of intermediate brightness. Spectral analysis of the area inside the border, which includes areas with all three brightness levels, shows a large concentration of carbon and a small amount of Cu, both presumably from the Cu-supported holey carbon TEM grid. Pd and O are present, as expected, but there is also a substantial signal for Si, and much more O than could be accounted for even if the particles were solid PdO.

Image B shows a higher magnification image of another group of particles, with the EDX spectrum taken from a small spot in the center of the brightest particle, as indicated by the red circle. Other than C and Cu from the TEM grid, this spot is composed of mostly Pd, with O and Si both present at about one-third the Pd concentration.

Image C shows the same particle aggregate as in B but with the EDX analysis area chosen to sample one of the intermediate contrast regions near the edge of the aggregate. Lower contrast could indicate a part of the aggregate that is simply thinner or a part where the concentration of high Z elements is lower. The

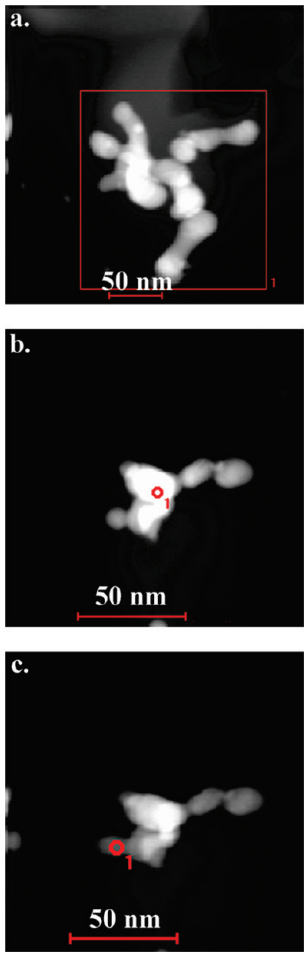

Figure 4. STEM/HAADF images of $(THD)_2$ catalyst after passage through reactor at 500 °C. (a) Lower magnification overview of a cluster of particles, corresponding atomic composition taken from area within box shown below; (b) higher magnification image of another group of particles, spectrum taken on center of particle; (c) same group of particles as in (b), spectrum from edge of particles.

EDX spectra show that the latter interpretation is correct. This region is Pd-free, and aside from C and Cu from the grid, is composed entirely of Si and O in a 1:1.5 ratio. To minimize sampling bias with the STEM/EDX work, analysis of several other particles and particle aggregates was carried out, with similar results.

The surprise in these images was the presence of Si-rich regions. The amount of Si in the spectra is far too high to be attributed to internal fluorescence from the dead layer of the detector,[37] and the O concentration seems to vary with the concentration of Si rather than Pd. Taken together with the HRTEM imagery, the conclusion is that the material exiting the reactor includes Pd-rich primary particles that are mostly crystalline, metallic Pd, as well as a distribution of particles composed of partially oxidized silicon (see below for discussion of SiO_x chemical state). The nature of the Pd−SiO_x interaction is of some importance, because it has been shown that Pd-silica interactions can reduce activity.[43] Fortunately, as discussed in the following section, comparison of the TEM and new, high dilution SMPS data suggests that the particles are mostly independent in the reactor, and aggregate extensively only as they are deposited on the TEM grids. In that case, the SiO_x particles should have little if any effect on the Pd particle activity.

Because all the other reactants are pure gases, we suspected that the source of the Si contamination was in the atomizer or $Pd(THD)_2$/toluene solution. To test this hypothesis, two control experiments were conducted with flow conditions identical to those above and with TEM grids positioned to collect any nanoparticulate products. In one experiment, N_2 was flowed through the empty atomizer, then into the normal flow mixture in the reactor. In the second, the atomizer was loaded with toluene (J.T. Baker 99.7% purity) that was atomized and carried by the N_2 into the main reactor. STEM/EDX analysis showed that with no toluene in the atomizer, essentially no particles deposited on the TEM grid, but with toluene in the atomizer, Si-rich material was deposited on the grid. It is unclear if the Si is a contaminant of the toluene itself or if toluene is dissolving Si from the glass atomizer. Even though the SiO_x particles do not appear likely to influence the chemistry, for future experiments, we will switch solvents or fabricate a metal atomizer, as needed, to eliminate this contaminant.

B. After Passage through the Reactor at 700 °C. Similar particle collection/analysis experiments were carried out for material produced in methane-free flows at a 700 °C reactor temperature. This temperature is just above the point where catalytic ignition was observed in methane-containing flows, thus comparison with the particles collected at 500 °C is of interest in understanding the factors controlling ignition. At 700 °C, it was observed that there was a threshold concentration of Pd required for ignition, of $\sim 4.5 \times 10^{-4}$ mol of Pd per mole of CH_4. Figure 5 shows a large area TEM image of these particles with accompanying size distributions, comparing TEM and SMPS results. As comparison with Figure 1 shows, both the appearance of the particles in the image and the extracted TEM size distribution are nearly identical to the corresponding 500 °C results.

The presence of aggregates in the TEM images, and the report by Shimizu et al.[6] of SMPS size distributions averaging ~25 nm—considerably larger than the TEM *primary* particles—raises the issue of whether the Pd particles are already aggregated in the reactor or if aggregation takes place after the reactor, in the course of collecting particles for TEM collection or transferring the particle stream for SMPS analysis. For the present SMPS measurements, we employed a Venturi-like probe directly inserted through the reactor wall, to give a more rapid dilution of the stream being sampled into the SMPS. Figure 5 shows that the resulting SMPS size distribution is quite similar to that measured for *primary* particles by TEM. The similarity indicates that the gas flow in the reactor was nearly free of aggregates, and that the aggregation seen in the TEM and in the old SMPS setup must have occurred after the reactor, as the particles were sampled. The shift of the TEM distribution to slightly smaller sizes compared to the SMPS results is attributed to sampling bias. Particles were collected for TEM by diffusion to the grid; thus, a bias toward smaller particles is expected. Nonetheless, it is clear that both aggregation in the gas phase and sampling bias are minor effects for these conditions. In that case, the ignition chemistry should be essentially unaffected by aggregation

Figure 6a shows a characteristic SAED pattern for the 700 °C sample, and Figure 6b shows a high-resolution image of a typical small ~10 nm particle with lattice fringes. Both the diffraction spacings (Table 1) and the collection of images of particles formed at 700 °C are quite similar to the analogous results for the 500° sample. In both cases, the bulk of the Pd particles is crystalline metallic Pd. STEM/EDX data were also collected for the 700 °C sample but are not shown because, again, they are virtually identical to those obtained from the 500 °C sample (including the SiO_x contamination).

TABLE 3: XEDS Results

XEDS atomic composition								
image A			image B			image C		
element	atomic %	uncertainty %	element	atomic %	uncertainty %	element	atomic %	uncertainty %
Pd(K)	2.4	1.0	Pd(K)	21.2	0.4	Pd(K)	–	–
O(K)	13.2	0.5	O(K)	6.9	0.1	O(K)	17.0	0.3
C(K)	70.6	0.2	C(K)	58.4	0.3	C(K)	56.6	0.8
Si(K)	12.4	1.0	Si(K)	7.1	0.1	Si(K)	25.3	0.4
Cu(K)	1.5	1.0	Cu(K)	6.3	0.1	Cu(K)	1.0	0.1

Summary of Microscopy Results. The microscopy data show that the size distribution of primary nanoparticles and the composition of the particles are similar for reactor temperatures above and below the ignition point. A few experiments were carried out for flows containing aerosols with different $Pd(THD)_2$ concentrations. One might expect that a higher Pd concentration in the gas mixture might lead to formation of larger particles. Instead, we observed more particles, but with about the same distribution of primary particle sizes. There is also more aggregation during deposition on the TEM grids, as expected for higher particle density. Because the gas is diluted and quenched by cold N_2 before the TEM collection, the particles on the grid should not undergo the sort of sintering behavior observed by Datye et al. in a study of supported Pd catalysts.[44]

In all samples, the primary catalyst particles have bulk structures of crystalline metallic Pd, with a size distribution peaking at ~8 nm. The dominance of Pd, rather than PdO, is somewhat surprising considering that PdO is the thermodynamically favored phase under the low temperature/oxidizing conditions where the particles were formed. Given that PdO is also the more catalytically active state for methane combustion,[8,11,45] it seems worthwhile to examine the surface chemistry of the particles to see if it differs significantly from the particle bulk.

X-ray Photoelectron Spectroscopy. XPS is sensitive to the top few nanometers of the sample surface, providing a means to look for chemical modification of the particle surfaces. Figure 7 shows XPS spectra collected for both the 500 and 700 °C samples. The samples were collected on TEM grids in the same

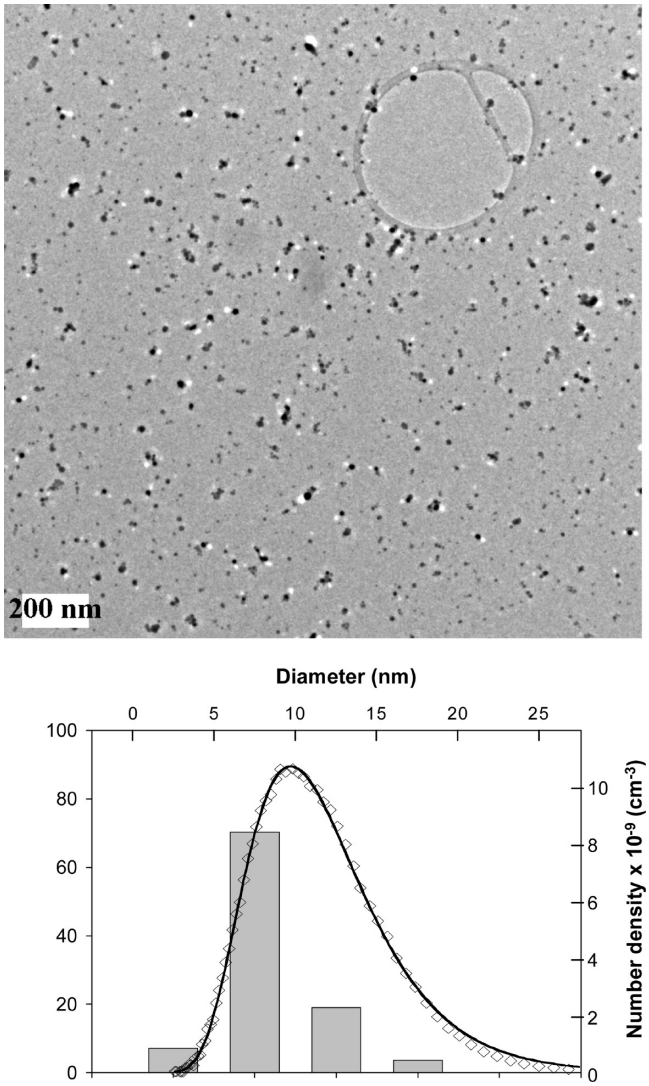

Figure 5. (Top) Low-magnification TEM image of $Pd(THD)_2$ catalyst after passage through reactor at 700 °C. (Bottom) Corresponding size distributions determined from TEM (bars) and from a scanning mobility particle sizer (SMPS - symbols and lines).

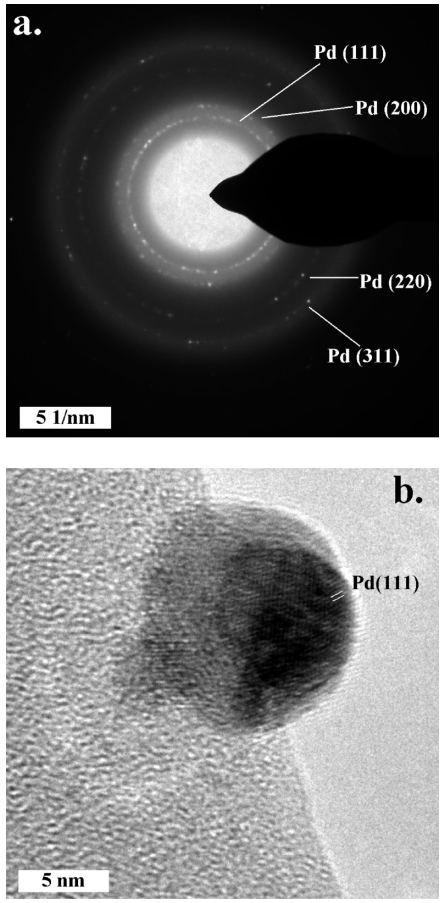

Figure 6. (a) SAED pattern for $Pd(THD)_2$ catalyst after passage through reactor at 700 °C; (b) typical small particle with Pd(111) fringes visible.

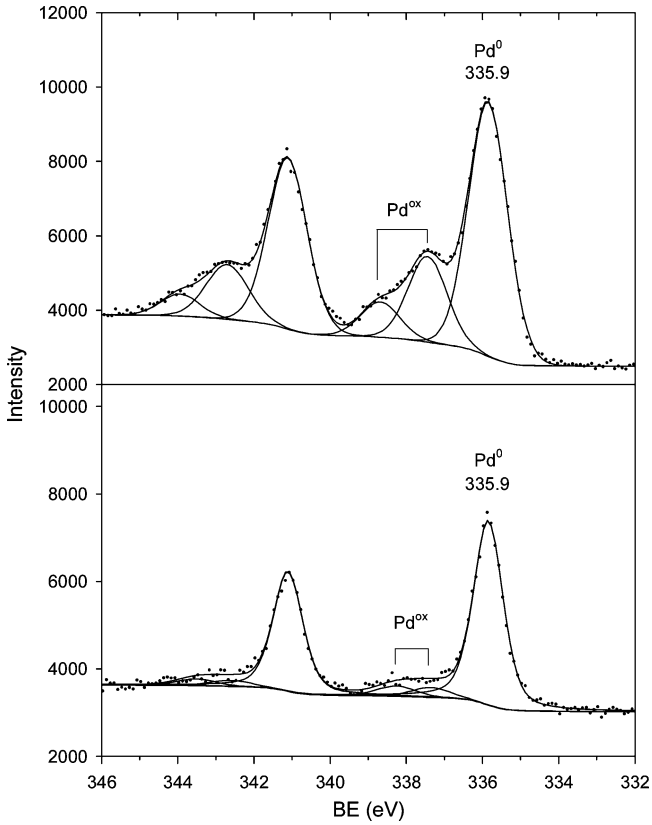

Figure 7. Pd 3d photoelectron spectra for particles passing through reactor at 700 (top) and 500 °C (bottom).

manner as was done for the microscopy experiments, with the only difference being higher particle density to obtain better signal-to-noise ratio to aid chemical state identification. The spectra were analyzed by subtracting a Shirley background, then fitting with Gaussian/Lorentzian functions.

In the 700 °C spectrum, each fine structure component has three peaks, at 335.9, 337.4, and 338.7 eV for the main $3d_{5/2}$ component. The largest peak (335.9 eV) is in reasonable agreement with the literature binding energy (335.7)[46] for metallic Pd and will be denoted Pd^0. Given the microscopy results above, the obvious conclusion is that this Pd^0 signal represents the bulk (interior) of the particles. The small shift from the literature value may result from sample charging or possibly is a final state effect due to less efficient core hole screening in the nanoparticles as compared to bulk Pd. This phenomenon has been previously observed in a XPS study of small Pt and Pd clusters.[47] The smaller peak shifted 1.5 eV to higher binding energy is clearly from some oxidized Pd species, which we will denote Pd^{ox}. The shift of the Pd^{ox} peak is intermediate between the shifts expected for PdO (336.9 eV)[48] and PdO_2 (337.7 eV).[49] The high-binding-energy region of the experimental peak is asymmetrically broadened, which was fit by adding a small peak at 338.7 eV. The origin of this high-energy broadening is not clear. Photoemission spectra of metal oxides often have shakeup features shifted to higher binding energies from the main peaks, and Militello et al. reported a shakeup satellite in their study of PdO powder.[50] However, they found the peak position of this satellite to be 339.8 eV—well above the energy of our high energy tail. It is also possible that the high energy peak results from a higher oxidation state of Pd; however, the energy extends well above the range expected for PdO_2. For the purposes of quantitating the amount of oxidized Pd present, we simply consider all intensity outside the metallic Pd^0 peak to be oxidized Pd, Pd^{ox}.

Taking the XPS and TEM results together, it is clear that while the bulk (interior) of the nanoparticles formed at 700 °C is metallic Pd, there is an oxidized surface layer. For the 500 °C sample, the Pd^{ox} signal is barely detectable, indicating formation of much less surface oxide. It is possible to estimate the thickness of the oxide layer by modeling the ratio of Pd^{ox} to Pd^0 signals. The particles are small enough that the X-rays fully penetrate the sample, thus the detection sensitivity of material in different regions of the sample is determined by the electron detection probability. The effective attenuation length (EAL) of Pd photoelectrons in Pd (1.34 nm) and PdO (1.41 nm) can be estimated using the NIST Electron Effective Attenuation Length database program.[51] Electrons generated in different locations within a particle are detected with efficiency that decays exponentially with the path length (d) required to escape in the direction of the detector: $\exp(-d/\mathrm{EAL})$. We modeled the XPS intensities expected for a single spherical particle, and also for a randomly packed group of spherical particles. In each case, the particles were assumed to have ~8 nm diameter, and the thickness of the oxide layer was varied to fit observed ratio of the Pd^{ox}/Pd^0 XPS intensities. For either model, the Pd^{ox}/Pd^0 ratio is is ~2.4 times greater than it would be for a oxide-covered planar Pd surface. This enhanced sensitivity to the surface oxide results partly from the curvature of the particles and partly from the fact that some signal from the far side of the particles penetrates through the bulk to be detected.

On the basis of the observed intensity ratios, the oxide layer is estimated to be ~0.36 nm thick for the 700 °C sample and 0.09 nm thick for the 500 °C sample, assuming a uniform oxide layer over the particle surfaces. 0.36 nm corresponds to essentially one monolayer of oxidized Pd on the particle surfaces at 700 °C and partial monolayer coverage at 500 °C. These oxidized Pd layers are too thin to observe in the TEM images and are probably not ordered well enough to contribute to structure in the electron diffraction patterns. The fact that only a single monolayer of oxide forms at 700 °C could simply reflect the slow oxidation kinetics, but it may be that once the first monolayer forms, it inhibits oxidation of the bulk, as found by Datye et al., in a study of Pd/PdO particles on alumina supports.[41]

In addition to the Pd oxidation state, we also used XPS to characterize the chemical state of the silicon contaminant. Details are in the Supporting Information, but briefly, the Si is all found to be oxidized, with binding energy in the range between those typically observed for silicates and silica. In the discussion above, we therefore simply referred to the silica as SiO_x. Because of the huge C and Cu signals from the grids, and a presumed contribution from adventitious adsorbates, the only useful information in the elemental intensity ratios is the relative amount of Pd and Si in the samples. The raw Pd/Si ratios are ~24.3 and 20.4 for the 700 and 500 °C samples, respectively. After correction for the atomic sensitivities, these correspond to a roughly 3:2 ratio of Pd/Si.

Conclusions: Catalyst Particle Formation and Activation

Particles collected at reactor temperatures below (500 °C) and above (700 °C) the temperature where catalytic ignition was observed for methane-containing flows were found to have essentially identical size distributions and particle morphologies with one important exception. Those collected above the ignition temperature were found to have ~1 monolayer of oxidized palladium on their surfaces, whereas particles collected below the ignition temperature had little oxide present. The similarity

in other particle properties presumably reflects a particle formation mechanism in which the $Pd(THD)_2$ decomposes, and Pd nanoparticles condense as the precursor is carried into the furnace, and the carrier gas heat up. Evidently, at 500 °C, the kinetics of Pd oxidation are sufficiently slow that not even a monolayer of oxidized Pd forms during the ~ 1 s flow tube residence time. By 700 °C, the Pd oxidation kinetics are fast enough to form a monolayer of oxidized Pd, and this oxidation appears to activate the particles for methane ignition. This conclusion has implications for use of such organometallic precursors for in situ ignition catalysis. The flow and temperature profiles must be such that the particles have time to oxidize, before significant catalytic ignition can be expected.

Acknowledgment. The Utah and USC groups gratefully acknowledge support for this work from the Air Force Office of Scientific Research through the MURI program (FA9550-08-1-0400). The Utah, USC, TDA, and Reaction Systems efforts were also supported by AFOSR STTR and AFRL SBIR contracts to develop fuel soluble catalysts for hydrocarbon fuels (FA9550-07-0106 and FA8650-06-C-2673, respectively).

Supporting Information Available: Si 2p X-ray photoelectron data. This material is available free of charge via the Internet at http://pubs.acs.org.

References and Notes

(1) Ciuparu, D.; Lyubovsky, M. R.; Altman, E.; Pfefferle, L. D.; Datye, A. *Catal. Rev. Sci. Eng.* **2002**, *44*, 593.
(2) Edwards, T. *Combust. Sci. Technol.* **2006**, *178*, 307.
(3) Lewis, M. J. *J. Propulsion Power* **2001**, *17*, 1214.
(4) Nabity, J.; Engel, J.; Cook, R.; Yu, J.; Anderson, S.; Wickham, D. *Catalysts to Improve Jet Fuel Combustion & Heat Sink Capacity*; AFOSR Molecular Dynamics Conference, 2008, Washington, DC.
(5) Wickham, D. T.; Cook, R.; Voss, S.; Engel, J. R.; Nabity, J. *J. Russ. Laser Res.* **2006**, *27*, 552.
(6) Shimizu, T.; Abid, A. D.; Poskrebyshev, G.; Wang, H.; Nabity, J.; Engel, J.; Yu, J.; Wickham, D.; Van Devener, B.; Anderson, S. L.; Williams, S. Combust. Flame 2009, doi:10.1016.
(7) Farrauto, R. J.; Hobson, M. C.; Kennelly, T.; Waterman, E. M. *Appl. Catal. A* **1992**, *81*, 227.
(8) McCarty, J. G. *Catal. Today* **1995**, *26*, 283.
(9) Lyubovsky, M.; Pfefferle, L. *Catal. Today* **1999**, *47*, 29.
(10) Corro, G.; Vazquez-Cuchillo, O.; Banuelos, F.; Fierro, J. L. G.; Azomoza, M. *Catal. Commun.* **2007**, *8*, 1977.
(11) Han, J.; Zemlyanov, D. Y.; Ribeiro, F. H. *Catal. Today* **2006**, *117*, 506.
(12) Yoshida, H.; Nakajima, T.; Yazawa, Y.; Hattori, T. *Appl. Catal. B* **2007**, *71*, 70.
(13) Nasibulin, A. G.; Richard, O.; Kauppinen, E. I.; Brown, D. P.; Jokiniemi, J. K.; Altman, I. S. *Aerosol Sci. Technol.* **2002**, *36*, 899.
(14) Keskinen, H.; Maekelae, J. M.; Vippola, M.; Nurminen, M.; Liimatainen, J.; Lepistoe, T.; Keskinen, J. *J. Mater. Res.* **2004**, *19*, 1544.
(15) Schuyten, S.; Dinka, P.; Mukasyan, A. S.; Wolf, E. *Catal. Lett.* **2008**, *121*, 189.
(16) Chiarello, G. L.; Ferri, D.; Grunwaldt, J.-D.; Forni, L.; Baiker, A. *J. Catal.* **2007**, *252*, 137.
(17) Fraga, M. A.; Greca, M. C.; Appel, L. G. *ACS Symp. Ser.* **2003**, *852*, 375.
(18) Govindraj, B.; Basavaraja, S.; Bedre, M. D.; Venkataraman, A. *Mater. Sci.* **2009**, *5*, 36.
(19) Hannemann, S.; Grunwaldt, J.-D.; Lienemann, P.; Guenther, D.; Krumeich, F.; Pratsinis, S. E.; Baiker, A. *Appl. Catal. A* **2007**, *316*, 226.
(20) Specchia, S.; Finocchio, E.; Busca, G.; Palmisano, P.; Specchia, V. *J. Catal.* **2009**, *263*, 134.
(21) Specchia, S.; Vella, L. D.; Burelli, S.; Saracco, G.; Specchia, V. *ChemPhysChem* **2009**, *10*, 783.
(22) Strobel, R.; Pratsinis, S. E.; Baiker, A. *J. Mater. Chem.* **2005**, *15*, 605.
(23) Adak, L.; Chattopadhyay, K.; Ranu, B. C. *J. Org. Chem.* **2009**, *74*, 3982.
(24) Laksmikanta, A.; Kalicharan, C.; C, R. B. *J. Org. Chem.* **2009**, *74*, 3982.
(25) Han, W.; Liu, C.; Jin, Z.-L. *Org. Lett.* **2007**, *9*, 4005.
(26) Illa, O.; Rodriguez-Garcia, C.; Acosta-Silva, C.; Favier, I.; Picurelli, D.; Oliva, A.; Gomez, M.; Branchadell, V.; Ortuno, R. M. *Organometallics* **2007**, *26*, 3306.
(27) Jiang, J.-Z.; Cai, C. J. Colloid Interface Sci. 2006, *299*.
(28) Saha, D.; Chattopadhyay, K.; Ranu, B. C. 2009, *50*, 1003.
(29) Tao, L.; Xie, Y.; Deng, C.; Li, J. *Chin. J. Chem.* **2009**, *27*, 1365.
(30) Wang, W. L.; Wang, Y. Y.; Wan, C. C.; Lee, C. L. *Colloids Surf. A* **2006**, *275*, 11.
(31) Bi, X.-z.; Jiang, Z.-q.; Huang, W.-x. *Zhongguo Kexue Jishu Daxue Xuebao* **2008**, *38*, 701.
(32) Evans, G.; Kozhevnikov, I. V.; Kozhevnikova, E. F.; Claridge, J. B.; Vaidhyanathan, R.; Dickinson, C.; Wood, C. D.; Cooper, A. I.; Rosseinsky, M. J. *J. Mater. Chem.* **2008**, *18*, 5518.
(33) Kunimatsu, K.; Sato, T.; Uchida, H.; Watanabe, M. *Langmuir* **2008**, *24*, 3590.
(34) Thompson, J.; Vasquez, A.; Hill, J. M.; Pereira-Almao, P. *Catal. Lett.* **2008**, *123*, 16.
(35) Yang, Y.; Saoud, K. M.; Abdelsayed, V.; Glaspell, G.; Deevi, S.; El-Shall, M. S. *Catal. Commun.* **2006**, *7*, 281.
(36) Yoosuk, B.; Kim, J. H.; Song, C.; Ngamcharussrivichai, C.; Prasassarakich, P. *Catal. Today* **2008**, *130*, 14.
(37) Williams, D. B.; Carter, C. B. *Transmission Electron Microscopy-A Textbook for Materials Science*; Plenum Press: New York, London, 1996.
(38) Penner, S.; Wang, D.; Jenewein, B.; Gabasch, H.; Klotzer, B.; Knop-Gericke, A.; Schlogl, R.; Hayek, K. *J. Chem. Phys.* **2006**, *125*, 094703/1.
(39) Roberts, W. L.; Campbell, T. J.; Rapp, G. R. *Encyclopedia of minerals*, 2nd ed.; Van Nostrand Reinhold: New York, 1990.
(40) Rao, Y. K. *Stoichiometry and Thermodynamics of Metallurgical Processes*; Cambridge University Press: Cambridge, UK, 1985.
(41) Datye, A. K.; Bravo, J.; Nelson, T. R.; Atanasova, P.; Lyubovsky, M.; Pfefferle, L. *Appl. Catal. A* **2000**, *198*, 179.
(42) Bayer, G.; Wiedemann, H. G. *Thermochim. Acta* **1975**, *11*, 79.
(43) Zhu, G.; Fujimoto, K.-I.; Zemlyanov, D. Y.; Datye, A. K.; Ribeiro, F. H. *J. Catal.* **2004**, *225*, 170.
(44) Datye, A. K.; Xu, Q.; Kharas, K. C.; McCarty, J. M. *Catal. Today* **2006**, *111*, 59.
(45) Grunwaldt, J.-D.; van Vegten, N.; Baiker, A. *Chem. Commun.* **2007**, 4635.
(46) Hufner, S.; Wertheim, G. K. *Phys. Rev. B* **1975**, *11*, 678.
(47) Cheung, T. T. P. *Surf. Sci.* **1984**, *140*, 151.
(48) Barr, T. L. *J. Vac. Sci. Technol. A* **1991**, *9*, 1793.
(49) Briggs, D.; Seah, M. P. *Practical Surface Analysis*, 2nd ed.; Wiley: Chichester, 1990; Vol. 1.
(50) Militello, M. C.; Simko, S. J. *Surf. Sci. Spectra* **1997**, *3*, 395.
(51) Powell, C. J.; Jablonski, A. *NIST Electron Effective Attenuation Length Database Version 1.1*; NIST: Gaithersburg, MD, 2003.

JP904317Y